Electrochimica Acta 309 (2019) 264–273

Contents lists available at ScienceDirect

Electrochimica Acta

journal homepage: www.elsevier.com/locate/electacta

Material structure and chemical bond effect on the electrochemical performance of black phosphorus-graphite composite anodes

Hosop Shin [a, 1], Jianyu Zhang [a], Wei Lu [a, b, *]

[a] Department of Mechanical Engineering, University of Michigan, Ann Arbor, MI, 48109, USA
[b] Department of Materials Science and Engineering, University of Michigan, Ann Arbor, MI, 48109, USA

ARTICLE INFO

Article history:
Received 17 February 2019
Received in revised form
21 March 2019
Accepted 21 March 2019
Available online 23 March 2019

Keywords:
Li-ion battery
Black phosphorus
Phosphorus-carbon composite
Degradation mechanism
Fracture
Pulverization

ABSTRACT

Black phosphorus (BP) is a little-studied but promising next-generation anode material for high-energy density Li-ion and Na-ion batteries. To understand the relationship between material property and electrochemical performance, black phosphorus-graphite (BP-G) composite materials are synthesized with two different BP-G molar ratios. This study demonstrates that the crystal structure and P–C bond of BP-G composites are affected by the BP-G molar ratio, which are directly correlated to cycle stability and the lithiation/delithiation process. $BP_{0.9}G_1$ shows a medium-range ordered structure, retaining some features of BP and having fewer or weaker P–C bonds. In contrast, $BP_{0.3}G_1$ has an amorphous-like structure with robust P–C bonds, which is helpful in withstanding the large volume change upon lithiation or delithiation. As a result, fracture and pulverization of particles, which are clearly seen in $BP_{0.9}G_1$ electrode, are scarcely observed in the cycled $BP_{0.3}G_1$ electrode. The possibility of mechanical failure in the BP-based electrode induced by BP's hydrophilic nature and the formation of Cu_3P is also discussed. This work not only contributes to improving the current understanding of phosphorus-based anodes, but also provides direct evidence of fracture and pulverization of BP particles during cycling.

1. Introduction

Black phosphorus (BP) is an excellent candidate to be a next-generation anode material for both lithium-ion and sodium-ion batteries, enabling high energy density battery systems. It has a theoretic specific capacity of 2,596 mAh/g, which is significantly higher than the capacity of current generation anodes (graphite, 372 mAh/g) and is close to that of a silicon anode. Depending on the quality, BP exhibits a moderate electrical conductivity (0.1–5.6 S/cm) [1,2]. In addition, an important cell design property for a high-energy density battery system is the intrinsic material density of the active material. BP's density is 2.69 g/cm^3, which is higher than silicon (~2.33 g/cm^3) and graphite (~2.27 g/cm^3) [2]. In contrast to alloying anode materials (such as tin and silicon), the benefit of BP is its use as an anode material for sodium-ion batteries due to the favorable intercalation of Na-ions into BP. This is largely due to BP's puckered 2D layered structure, similar to graphite but with a larger interlayer spacing (0.54 nm), which enables it to accommodate large ions. However, Na-ions do not electrochemically insert into a silicon anode [3].

Phosphorus exists in a number of allotropic forms (white, red, violet, and black) and BP is thermodynamically the most stable form among them, and exhibits rhombohedral, orthorhombic, and cubic metallic phases depending on synthesis temperature/pressure conditions [4]. BP has the advantages of direct band gap (0.3 eV for its bulk form), high carrier mobility (typically higher than 200 cm^2/(V s)), and considerable catalytic activities, thereby it has also attracted significant attentions in the fields of optoelectronics, photocatalysis, and photovoltaics [5,6].

Although several efforts have been made to use red phosphorus (RP) for batteries [3,7–10], the direct use of RP in a practical battery is limited due to safety concerns. RP is more flammable than BP and can be easily ignited at moderate temperatures when exposed to air. In addition, heated RP in the presence of moisture creates phosphine gas, which is both highly flammable and toxic. These reactive or unstable characteristics of RP would be problematic in manufacturing battery electrodes. Moreover, RP has an amorphous

* Corresponding author. Department of Mechanical Engineering, Department of Materials Science and Engineering, University of Michigan, Ann Arbor, MI, 48109, USA.
E-mail address: weilu@umich.edu (W. Lu).
[1] Present address: Department of Mechanical and Energy Engineering, Indiana University-Purdue University Indianapolis (IUPUI), IN 46202, USA.

https://doi.org/10.1016/j.electacta.2019.03.149
0013-4686/

structure with poor bulk conductivity (1×10^{-14} S/cm), which negatively affects its battery applications [4].

Despite the potential impact of BP as an alternative anode material, relatively little research has been done in the battery field. This is mainly due to the requirement of precisely controlled high-temperature and high-pressure conditions under which BP is produced, as well as the limited electrochemical activity of synthesized BP. Park et al. pioneered research into the synthesis of BP using high-energy mechanical milling (HEMM) for battery applications [11]. With the HEMM process, the pressure and temperature in the reaction vessel can reach approximately 6 GPa and 200 °C, respectively [1,11]. They showed that BP phase transformation occurs sequentially as BP, LiP, Li_2P, and Li_3P upon lithiation. They also suggested that the excellent cycle performance of black phosphorus-carbon composite can be achieved by controlling the voltage range, which inhibits the formation of Li_3P. Although HEMM synthesis is simple and easy to implement, there is an inherent limitation in controlling the reaction condition precisely. Sun et al. implemented a high-pressure and high-temperature (HPHT) method using a cube-shaped pressure-transmitting medium and demonstrated that the BP prepared using their method exhibits a higher electrochemical reactivity for Li insertion than BP produced by the HEMM method [1]. They emphasized that a better quality of BP in terms of electrochemical reactivity can be produced by precisely controlling the synthetic condition.

A few studies have examined the electrochemical performance of pure BP and it was typically shown that the first-cycle coulombic efficiency is very low and the reversible capacity drops rapidly [1,11,12]. This is because the intrinsic electronic conductivity is not sufficient and a large volume change caused by Li_3P formation induces mechanical cracking and crumbling of BP. The *in-situ* and *ex-situ* transmission electron microscopy (TEM) studies revealed that BP experiences an anisotropic volume change, which was approximately 77% (for delithiation process) and 92% (for sodiation process) [13,14]. Although it remains unclear whether BP cracking and pulverization occur during lithiation or delithiation process, it is commonly accepted that the failure mechanism of BP is related to the lattice expansion/contraction [14].

To improve the electrochemical performance of BP-based anode materials, phosphorus-carbon composites have typically been synthesized using two synthetic routes. One approach is to confine nano-sized phosphorus into a porous carbon or mesoporous carbon matrix using a vaporization/adsorption strategy [7,9,15,16]. It was reported that the properties (such as pore volume, specific surface area, and particle size) of carbon determine the extent of phosphorus adsorption as well as chemical bonding between carbon and phosphorus, which ultimately affect the electrochemical performance of the composites. This strategy is typically suitable to synthesize P–C composites with a low ratio of P and it is difficult to control the content of P in the composite precisely. The other approach is to synthesize a chemically bonded composite structure using a facile ball-milling process [2,8,11,17]. While the ball-milling process cannot avoid the destruction of carbon materials, it enables production of composites with a high ratio of phosphorus [3,8,10,11,17,18]. It was proposed that carbon structure plays an essential role in forming a stable P–C bond in the composite during the ball-milling process and graphite is the best choice for making phosphorous-carbon composites with long cycle life and high-rate capability [2]. It should be noted that the study used P–C composites with the P:C molar ratio of 1:3 (close to $P_{0.3}C_1$), which was much lower than the P:C composition (70:30 wt%, close to $P_{0.9}C_1$) typically used in most other studies [3,8,10,11,17]. Thus, it is still not clear whether the improvement of cycle life and rate capability is mainly attributed to the carbon source or BP:C composition.

In addition, although mechanical failure (cracking, crumbling, or pulverization) of phosphorous-carbon composites had been envisioned, there was no direct evidence showing the mechanical failure of BP-based anodes and fundamental studies to understand the degradation of BP-based anodes have rarely been conducted in the literature. This might be attributed to the fact that most researchers synthesized nanostructured phosphorus composites to better show electrochemical performance. With nanostructured phosphorus materials, it might be difficult to detect any mechanical degradation at the particle level.

The objectives of this study are to (1) systematically investigate how the electrochemical performance of black phosphorous-graphite (BP-G) composites is affected by BP:G composition, (2) identify the correlation between the material properties and electrochemical performance of BP-G composites, and (3) reveal the degradation mechanisms underlying the poor cycle life of BP-based anodes.

2. Experimental

2.1. Materials synthesis

All the materials were handled in an Ar-filled glove box (<1 ppm O_2 and H_2O). Material synthesis was also carried out in the glove box using a shaker-type milling machine (SPEX, 8000 M mixer/mill). There is possibility that the remaining RP after BP synthesis can be inversely transformed to white phosphorus, which is easy to self-ignite in the air at approximately 30 °C. Thus, material synthesis should be conducted carefully in an inert environment. To prepare the BP powder, RP powder (100 mesh, 98.9% purity, Alfa Aesar) was used as the starting material. Using the shaker mill, the HEMM process was conducted to synthesize BP powder from RP. The RP (6 g) was put into a hardened steel cylindrical vial (65 mL) with hardened steel balls (10 balls with a diameter of 12.7 mm and 18 balls with a diameter of 6.35 mm). The ball-to-powder mass ratio for BP synthesis was 17:1.

For BP-G composite synthesis, the BP synthesized by the HEMM process (6 h) was put into a hardened steel vial (65 mL) with graphite power (Timrex SLP30, Timcal), and then hardened steel balls (10 balls, 12.7 mm in diameter; 18 balls, 6.35 mm in diameter) were added to the vial. The ball-to-powder mass ratio was 25:1. The BP-G (4 g) composite was synthesized for 6 h using the same shaker mill. BP-G composites with different molar ratios were prepared: a low BP-ratio $BP_{0.3}G_1$ (43.6 wt% of BP and 56.4 wt% of graphite) and a high BP-ratio $BP_{0.9}G_1$ (69.9 wt% of BP and 30.1 wt% of graphite). The ratio of $BP_{0.9}G_1$ was chosen as many previous studies have suggested the molar ratio is the optimum composition that delivers the highest reversible capacity of BP-C composite [3,8,10,11,17,18]. The ratio of $BP_{0.3}G_1$ was selected based on a previous study in which excellent cycle performance of BP-C was achieved [2]. Although the study claimed the stable cyclability of BP-C was achieved due to the use of graphite as a carbon source [2], we speculated that BP-C composition might be the main reason for the improved cycling performance. To clearly study the effect of P:C composition on the electrochemical performance, we used a pristine graphite (Timrex SLP 30, Timcal) for both $BP_{0.3}G_1$ and $BP_{0.9}G_1$ composites.

2.2. Battery electrode fabrication

To prepare the BP-based anodes, a slurry was prepared by mixing the synthesized material (either BP/G or BP-G, 80 wt%) with a polyvinylidene fluoride (PvdF, Kureha 7298) binder (10 wt%) dissolved in *N*-methyl-2-pyrrolidone (NMP) and Super P (10 wt%) at 3000 rpm for 30 min using a SpeedMixer (DAC 150 FVZ double centrifugal mixer). The BP/G (mixture of BP and graphite) was prepared by mixing BP and graphite at 3000 rpm for 30 min using

the SpeedMixer. The resulting slurry was cast onto a 9 μm-thick copper (Cu) foil at a constant speed using a doctor-blade film coater (9 mils). The electrode was dried for 4 h in a vacuum oven at 110 °C. This electrode-drying step should be performed carefully to prevent any reaction between the Cu foil and BP. The electrode was punched into disks (10 mm in diameter). The thickness of the electrode (without Cu foil) was in the range of 50–70 μm and the electrode loading (total weight of BP and graphite) was approximately 3.5–4.0 mg/cm^2. The electrode disks were stored in an Ar-filled glove box to avoid exposure to moisture. To prevent the BP-based electrode from oxidation or degradation, storage in an inert atmosphere was required.

2.3. Cell fabrication/electrochemical tests/post-mortem analysis

2032-type coin cells (BP-based anodes/Li half cells) were assembled in an Ar-filled glove box. The electrolyte used for the cells was 1.0 M lithium hexafluorophosphate ($LiPF_6$) dissolved in a mixture (1:1, v/v) of ethylene carbonate (EC) and dimethyl carbonate (DMC). The cells were cycled using a Maccor cycler between 0.01 V and 2 V (vs. Li/Li$^+$) with a constant current charge/discharge protocol. To compare the cycle performance of $BP_{0.3}G_1$ with that of $BP_{0.9}G_1$, either the same current density (200 mA/g, based on the total weight of BP and graphite) or a similar C-rate was applied. Here, the C-rate was based on the theoretical capacity of each composite estimated by a simple mixing rule ($BP_{0.3}G_1$: 1352.24 mAh/g and $BP_{0.9}G_1$: 1929.7 mAh/g). Electrochemical impedance spectroscopy (EIS) measurement was performed using a Biologic VMP3 with an EIS module. The frequency was scanned from 250 kHz to 25 mHz using 5 mV amplitude perturbation. Before the EIS test, the cell voltage was held at 1.0 V (vs. Li/Li$^+$) for 2 h.

In post-mortem analysis, the cycled BP-based anodes were disassembled at the delithiated state (2.0 V vs. Li/Li$^+$) in an Ar-filled glove box and washed with DMC to remove residual salts remaining on the electrode. The electrode was dried for more than 8 h and put onto a scanning electron microscopy (SEM) pin stub mount in the glove box. All samples were quickly inserted into the SEM instrument (less than 1 min) to avoid sample contamination.

2.4. Material characterization

X-ray diffraction (XRD) patterns of synthesized samples were obtained by a Rigaku rotating anode instrument with a Cu Kα radiation source ($\lambda = 1.541$ Å). The XRD samples were prepared by grinding synthesized powder and then pressing the powder onto a glass substrate. The XRD patterns were collected over the 2θ range of 10°–80° using a scan speed of 0.8° per min and the increment was set to 0.02° per step. SEM images were taken using a Philips XL30 FEG (high-resolution images, accelerating voltage 20 kV). Raman spectroscopy characterization was conducted using a WITec alpha300 RA confocal Raman system with a laser wavelength of 532 nm. All Raman tests were performed at a low power level (approximately 2.5 mW) to avoid laser-introduced damage to the samples. To avoid any moisture effect, all samples were tested immediately after removal from the Ar-filled glove box. X-ray photoelectron spectroscopy (XPS) was conducted using a Kratos Axis Ultra X-ray photoelectron spectrometer equipped with a monochromatic Al Kα excitation source ($h\nu = 1486.6$ eV). The analyzed area was 300 × 700 μm^2. The binding energy scale was calibrated from intrinsic hydrocarbon contamination using the C 1s peak at 285 eV. Core spectra were recorded with 20 eV constant pass energy. The fitting of core peaks was performed using the Shirley background correction and Gaussian-Lorentzian curve synthesis (70% Gaussian, 30% Lorentzian). Charge neutralization was used during measurements. Electronic conductivity measurements were conducted using the four-point probe method. For conductivity measurements, BP/G and BP-G electrodes (80:10:10, active material:carbon black:PVDF wt%) were cast onto a glass plate. The electrode was dried at 110 °C for more than 8 h in a vacuum oven. A large size of the electrode (around 18 × 8 cm^2) was used to increase the accuracy of measurement. For each electrode, measurements were conducted five times at different locations.

3. Results and discussion

3.1. BP synthesis/characterization

The starting RP, an amorphous or low-range ordered structure, was successfully transformed to crystalline BP after the HEMM process (Fig. S1 of the Supplementary Information). The XRD pattern (Fig. S1a) of the synthesized BP showed a number of crystalline peaks, which was consistent with standard power diffraction data (JCPDS #01-073-1358). The synthesized BP was similar to those synthesized by other research groups [2,8,11,17], except for one [12]. The phase change from RP to BP was completed after just 1 h of the HEMM process, which was consistent with a previous study [18]. In our study, 6 h of HEMM process was selected as an optimal time to synthesize BP considering the level of BP's crystallinity, time-saving, and the level of contamination. It should be noted that the achievable degree of crystallinity of BP by HEMM synthesis was limited. A further increase of ball-milling time did not help to improve the crystallinity of BP. Raman spectra (Fig. S1b) also confirmed the phase transformation of RP to BP after 6 h of HEMM process. The synthesized BP showed three Raman active modes at 363, 438, and 467 cm^{-1}, which indicates that BP had an orthorhombic phase rather than a rhombohedral phase or a cubic phase [19].

A distinct difference in particle morphology was found between RP and BP (Fig. S2). While the RP showed particles with sharp edges, the synthesized BP displayed round-shaped coarse-fine particles. The large RP particles (below 150 μm) were broken down into smaller pieces while the phase transformation occurred. The synthesized BP was agglomerated to form secondary particles in which fine particles adhere to each other due to particle interaction during the HEMM process. Ball-milled fine particles have a strong tendency to agglomerate owing to their relatively large specific surface area and other properties. The synthesized BP encompassed a wide range of particle sizes (75 nm–71 μm) and the median D50 value was 5.7 ± 1.7 μm, which was much smaller than RP. Note that only 20% of the particles were shown as nano-size and most were micron-size particles. The BET surface area of the synthesized BP was 7.156 m^2/g, which was similar to the surface area of graphite (approximately 7.5 m^2/g) used for this study.

It is worthwhile to mention that we used micron-size BP to produce a chemically bonded BP-G composite, which was different from previous studies in which nanostructured phosphorus composites (e.g., nanoconfined phosphorus in a carbon matrix) were synthesized. This allowed us to directly observe the mechanical degradation phenomena that occur in the BP-based anode. Moreover, the use of micron-size BP is more realistic and practical in battery applications.

3.2. BP-G composite synthesis/characterization

To understand the difference in material characteristics of $BP_{0.9}G_1$ and $BP_{0.3}G_1$, synthesized BP-G composite materials were systematically characterized. As expected, $BP_{0.3}G_1$ contained more carbon element than $BP_{0.9}G_1$ (Fig. S3). Although relatively large particles were occasionally observed in $BP_{0.9}G_1$, there was no significant difference in the morphology and size of particles between

$BP_{0.9}G_1$ and $BP_{0.3}G_1$ materials. Distinct differences between $BP_{0.9}G_1$ and $BP_{0.3}G_1$ materials were observed in their crystal structures and chemical bonds, which will be demonstrated by the following Raman, XPS, and XRD results.

Fig. 1a shows the Raman spectra of pristine graphite and BP before the synthesis of BP-G composite. The synthesized BP powder displayed three Raman active modes at 363, 438, and 467 cm^{-1}, while the pristine graphite showed two characteristic D and G bands near 1350 and 1580 cm^{-1}, respectively. To characterize the extent of structural disorder in graphite, the peak intensity ratio I_D/I_G has been typically used [20]. Pristine graphite showed the dominant G-band peak with respect to the D-band peak (low I_D/I_G ratio), indicating a highly ordered graphite structure without defects. In contrast, BP-G composites showed much higher peak intensity ratios of I_D/I_G (i.e., the dominant D-band with respect to the G-band). This indicates that severe structural disordering occurred in the graphite when BP-G composites were produced by the HEMM process. During the HEMM process, particles of the BP/G powder mixture are subject to high energetic impact and mechanochemistry effect. The mixture particles are flattened and crushed by the compressive forces due to the collision of the milling balls and cluster of particles are impacted repeatedly with high kinetic energy. This induces not only creation of severely disordered carbon and phosphorous but also strong chemical reactions between as-milled BP and graphite particles. It is commonly known that the reactivity of as-milled solid particles increases during the high-energy ball milling process.

It is important to point out that the observed structural disordering was not only due to the structural destruction of graphite. Interestingly, a higher intensity ratio of D-band to G-band was observed in $BP_{0.9}G_1$ (1.53) compared to $BP_{0.3}G_1$ (1.41) (Fig. 1b). The difference in the degree of disordering indicates that the structure of $BP_{0.9}G_1$ could be different from $BP_{0.3}G_1$. $BP_{0.9}G_1$ had a more disordered carbon form or a less stable structure than $BP_{0.3}G_1$. The result suggests that BP-G composition determines the crystal structure of a BP-G composite, affecting the structural stability. A theoretical study was consistent with ours, supporting our finding [21].

Note that the BP-related signals (A^1_g, B^2_g and A^2_g) which represent P—P bond were no longer observed in both BP-G composites. There has been no agreement on the presence of BP Raman feature in BP-carbon composites. While Qian et al. [8] and Sun et al. [2] observed BP Raman feature in their composites, Kim et al. [3] and Ramireddy et al. [17] did not observe the feature. The absence of BP Raman signals in our BP-G composites might indicate that our BP-G has a composite structure similar to the phosphorous-carbon composites produced by Kim et al. and Ramireddy et al. [17]. Alternatively, the disappearance of BP-related Raman signals in BP-G composites might represent the breakup of P—P bonds in BP, creating P—C bonds in BP-G composites [2,8]. A previous study demonstrated that BP Raman signals in P/C composites were weakened and finally disappeared with increasing ball-milling time [8]. They explained that this is indicative of the strong interaction between phosphorus and carbon. Therefore, the synthesized $BP_{0.3}G_1$ and $BP_{0.9}G_1$ composites were believed to have the P—C bonds, which was further confirmed by the following XPS analysis.

As shown in Fig. 2, the deconvoluted XPS spectra (P 2p) of BP, $BP_{0.9}G_1$ and $BP_{0.3}G_1$ powders were compared to understand the formation of P—C bonds in BP-G composites. While BP powder exhibited only a P—P bond (129.9 eV and 130.8 eV assigned to $2p_{3/2}$ and $2p_{1/2}$, respectively), BP-G composites showed the co-existence of both a P—P bond and P—C bond (130.2 eV and 131.1 eV assigned to $2p_{3/2}$ and $2p_{1/2}$, respectively). The content (47.7%) of the P—C bond in the $BP_{0.3}G_1$ was much higher than that (17.1%) of the $BP_{0.9}G_1$. This suggests that more P—C bond formation existed in the structure of $BP_{0.3}G_1$ than $BP_{0.9}G_1$. It means that a different BP-G crystal structure with different chemical P—C bonds was formed depending on BP:G stoichiometry.

Based on our Raman and XPS analysis, the crystal structure of $BP_{0.3}G_1$ had a less disordered carbon form and consisted of more formation of P—C bonds than $BP_{0.9}G_1$. The structure of $BP_{0.3}G_1$ might be more robust in terms of structural stability than $BP_{0.9}G_1$. This could be closely related to the mechanical degradation/failure of BP-G composites.

According to previous density functional theory (DFT) calculation studies [21–23], there is preferred local bonding environment of carbon and phosphorus, and it is dependent on phosphorus/carbon composition. For instance, when phosphorus content is low in phosphorus carbide, the preferred type of structure is phosphorus-doped graphite [23]. In addition, formation of phosphorus carbides typically requires a significant number of weak P—P bonds. This reasonably explains why P—P bonds (or BP Raman signals) were not shown in BP-G composites. Our experimental results and the DFT predictions suggest that the synthesized BP-G composites had structures with P—C bonds but weak P—P bonds.

The crystal structural difference between $BP_{0.3}G_1$ and $BP_{0.9}G_1$ was further investigated by XRD analysis, as shown in Fig. 3. In the XRD pattern of $BP_{0.3}G_1$, the characteristic peaks related to

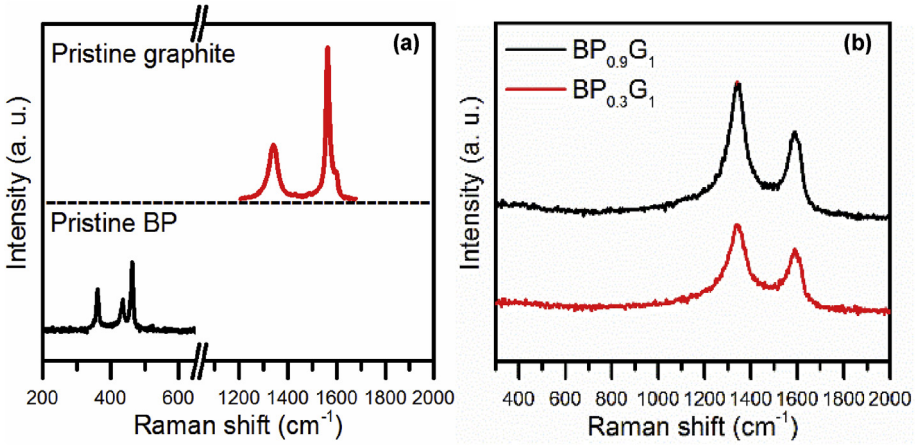

Fig. 1. Raman spectra of (a) pristine graphite and BP powder; (b) BP-G composite powder ($BP_{0.9}G_1$ in black; $BP_{0.3}G_1$ in red). (For interpretation of the references to colour in this figure legend, the reader is referred to the Web version of this article.)

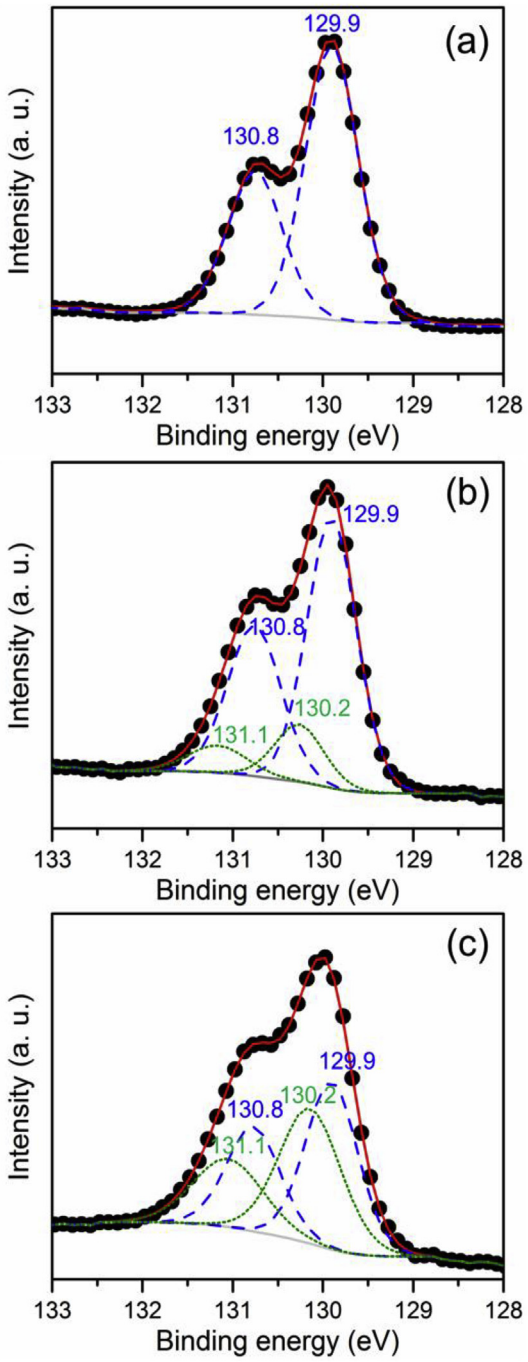

Fig. 2. Comparison of XPS spectra (P 2p) of (a) BP, (b) $BP_{0.9}G_1$, and (c) $BP_{0.3}G_1$ powders. Black dots, red solid lines, blue dashed lines, and green dashed lines represent the measurement data, the fitted XPS spectra, P–P bond doublets, and P–C bond doublets, respectively. (For interpretation of the references to colour in this figure legend, the reader is referred to the Web version of this article.)

orthorhombic BP (such as (020), (021), and (111) reflections) almost disappeared, which was due to the breakup of P–P bonds in BP and the creation of P–C bonds in $BP_{0.3}G_1$. Although the intensities of the characteristic peaks related to graphite, such as (002) and (101) reflections, marked as downside triangles in blue, were significantly diminished and broadened, these characteristic peaks remained. Moreover, these peaks shifted to lower 2θ angles with respect to the original (002) and (101) reflections. The decrease in the intensity of BP-related diffraction peaks and the shift of

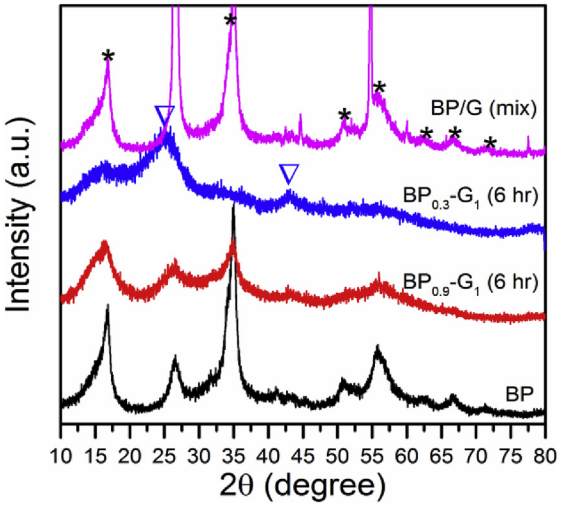

Fig. 3. XRD patterns of BP, BP-G composites ($BP_{0.9}G_1$ in red; $BP_{0.3}G_1$ in blue), and BP/G mixture (44:56 wt %). (For interpretation of the references to colour in this figure legend, the reader is referred to the Web version of this article.)

graphite-related peaks ((002) and (101) reflection) observed in $BP_{0.3}G_1$ might be attributed to the formation of new BP-G composite structure with P–C bonds.

In contrast, $BP_{0.9}G_1$ showed a different XRD pattern. The XRD pattern of $BP_{0.9}G_1$ still displayed the characteristic peaks related to BP but graphite-related diffraction peaks were relatively negligible. Thus, a different XRD pattern of $BP_{0.3}G_1$ compared with $BP_{0.9}G_1$ indicates $BP_{0.3}G_1$ had a different type of structure compared with the structure of $BP_{0.9}G_1$.

In summary, $BP_{0.3}G_1$ had an amorphous-type structure with robust P–C bonds, while $BP_{0.9}G_1$ had a medium-range ordered structure with fewer or weaker P–C bonds. It was speculated that $BP_{0.9}G_1$ was more brittle than $BP_{0.3}G_1$ since $BP_{0.9}G_1$ still retained the BP feature and BP was much harder than graphite. The amorphous-like structure with robust P–C bonds (i.e., $BP_{0.3}G_1$) could withstand large volume expansion during lithiation/delithiation, preventing any cracking or fracture. This is demonstrated in the next section.

The difference in crystal structure of $BP_{0.3}G_1$ and $BP_{0.9}G_1$ was further confirmed by the difference in their electrical conductivity. As shown in Fig. 4, the $BP_{0.3}G_1$ electrode (1.6×10^{-1} S/cm) showed approximately two times greater electrical conductivity than the $BP_{0.9}G_1$ electrode (8.9×10^{-2} S/cm). The structure type of $BP_{0.3}G_1$, which is close to phosphorus-doped graphite structure, is likely to have greater electrical conductivity than other types of

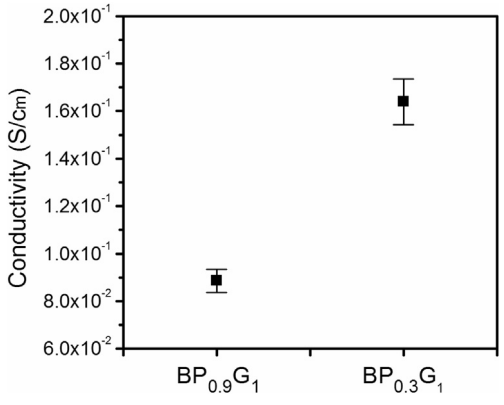

Fig. 4. Comparison of electrical conductivity of $BP_{0.9}G_1$ and $BP_{0.3}G_1$.

phosphorus-carbon structures because it retains the original graphite or graphene-like structure to some extent [23]. Thus, the difference in electrical conductivity between $BP_{0.3}G_1$ and $BP_{0.9}G_1$ might originate from their structural difference. It should also be mentioned that BP/G mixtures showed much greater electrical conductivity than the corresponding BP-G composites. BP/G (70:30 wt%) and BP/G (44:56 wt%) mixtures exhibited 1.4 and 4.9 S/cm, respectively. This indicates that BP and graphite were chemically bonded during the HEMM process, creating BP-G composites with completely different characteristics compared to BP or graphite.

Based on the above results, we conclude that $BP_{0.9}G_1$ exhibits a medium-range ordered structure which retains the original BP features somewhat and consists of weak P–C bonds. In contrast, $BP_{0.3}G_1$ has an amorphous and phosphorus-doped graphite-like structure with strong P–C bonds. In the next section, we demonstrate how the difference in the structural characteristics of BP-G composites caused by BP-G molar ratio is directly correlated to the difference in their electrochemical performance.

3.3. Cycle performance of BP-G composite and its degradation mechanism

To better understand the BP-G composite material, electrochemical performance was compared for BP/G (70:30 wt%) mixture, 1 h-HEMM and 6 h-HEMM synthesized $BP_{0.9}G_1$ composites. Fig. 5a shows the galvanostatic discharge-charge profiles of BP/G, 1 h-HEMM $BP_{0.9}G_1$, and 6 h-HEMM $BP_{0.9}G_1$ at the 1st cycle. Compared with the BP/G mixture, the first discharge capacity and cycle coulombic efficiency of 1 h-HEMM $BP_{0.9}G_1$ and 6 h-HEMM $BP_{0.9}G_1$ were significantly improved. The first discharge capacity of the BP/G mixture was 571 mAh/g, showing the first-cycle efficiency of only 16.1%. This indicates that a large portion of BP particles in the BP/G mixture did not participate in electrochemical reaction. Note that the electrical conductivity of BP/G mixture was much greater than the corresponding BP-G composite. This means that increasing electrical conductivity at the electrode level does not necessarily help making more BP particles to participate in electrochemical reaction.

Once BP and graphite were chemically bonded during the HEMM process to form a BP-G composite, the electrochemical performance was significantly enhanced. The first discharge capacity of 1 h-HEMM $BP_{0.9}G_1$ was 1126 mAh/g, showing a first-cycle efficiency of 64.5%. With increasing ball-milling time (6 h), the first discharge capacity of $BP_{0.9}G_1$ increased up to 1847 mAh/g, showing a first-cycle efficiency of 88.5%. The HEMM process contributed to increasing electrical conductivity of BP at the particle level by creating the BP-G composite. As a result, the enhanced electrochemical performance of $BP_{0.9}G_1$ was observed.

Although $BP_{0.9}G_1$ achieved a high discharge capacity and coulombic efficiency, severe capacity fade was still observed, as shown in Fig. 5b. The reversible capacity rapidly dropped within 30 cycles. The rapid capacity fade was consistent with a previous study, in which a different type of mill (either a planetary ball mill or magneto-ball bill) was used for synthesizing the $BP_{0.9}G_1$ composite [17]. Thus, the rapid capacity fade observed in $BP_{0.9}G_1$ might not be a synthesis issue but be an intrinsic material issue. As far as graphite is used as a carbon source for synthesizing phosphorus-carbon composite with 70 wt% of BP, the composite cannot avoid fast capacity fade. This might be correlated with the structural characteristics of $BP_{0.9}G_1$. The $BP_{0.9}G_1$, which exhibited a medium-range order structure with fewer and weaker P–C bonds, might be inherently vulnerable to large volume change during lithiation or delithiation, resulting in cracking and crumbling of BP-G particles.

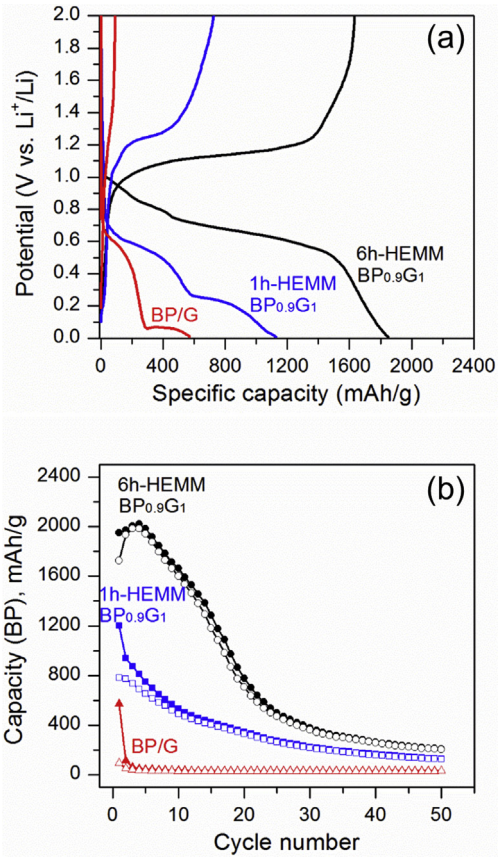

Fig. 5. (a) Galvanostatic discharge-charge profiles and (b) cycle performance of BP/G (70:30 wt%) mixture (red), 1 h-HEMM $BP_{0.9}G_1$ (blue), and 6 h-HEMM $BP_{0.9}G_1$ (black). Half-cells were cycled at a current density of 200 mA/g. Here, the capacity was calculated based on the weight of BP. Close and open symbols represent discharge and charge capacity, respectively. (For interpretation of the references to colour in this figure legend, the reader is referred to the Web version of this article.)

As shown in Fig. S4, the mechanical degradation of $BP_{0.9}G_1$ was responsible for the fast capacity fade. A number of fractured particles (marked with red arrows) were clearly found in the $BP_{0.9}G_1$ electrode after 50 cycles. The mechanical degradation (cracking, crumbling, and pulverization) of $BP_{0.9}G_1$ caused loss of electrical contact of active materials, thereby resulting in a rapid capacity fade. Note that the fractured particles were noticeably observed to be those with a relatively large size of 5–20 μm. This might be the reason why previous studies could not report any evidence of mechanical failure in the phosphorus-carbon composite. Since most previous studies have tried to confine nano-size phosphorous into a carbon matrix, it was difficult to characterize any possible fractures or cracks of the nano-size particles, although it is highly likely to happen. Alternatively, similar to the widely studied Si anodes, nano-size particles were likely to have less mechanical stress than micron-size particles upon cycling, thereby mitigating severe fracturing. The decrease of Si particle size to the nano-range has been known as an effective way to relieve any mechanical stress during a large volume expansion/contraction [24]. To the best of our knowledge, our study is the first report demonstrating direct evidence of mechanical failure of BP-G anodes.

Interestingly, cycle performance of BP-G composite was noticeably improved with a different BP-G composition ($BP_{0.3}G_1$). As shown in Fig. 6, $BP_{0.3}G_1$ showed much better cycle performance than $BP_{0.9}G_1$ (Fig. 6c). The excellent cycle stability of $BP_{0.3}G_1$ was attributed to the mechanical stability of $BP_{0.3}G_1$ electrode upon

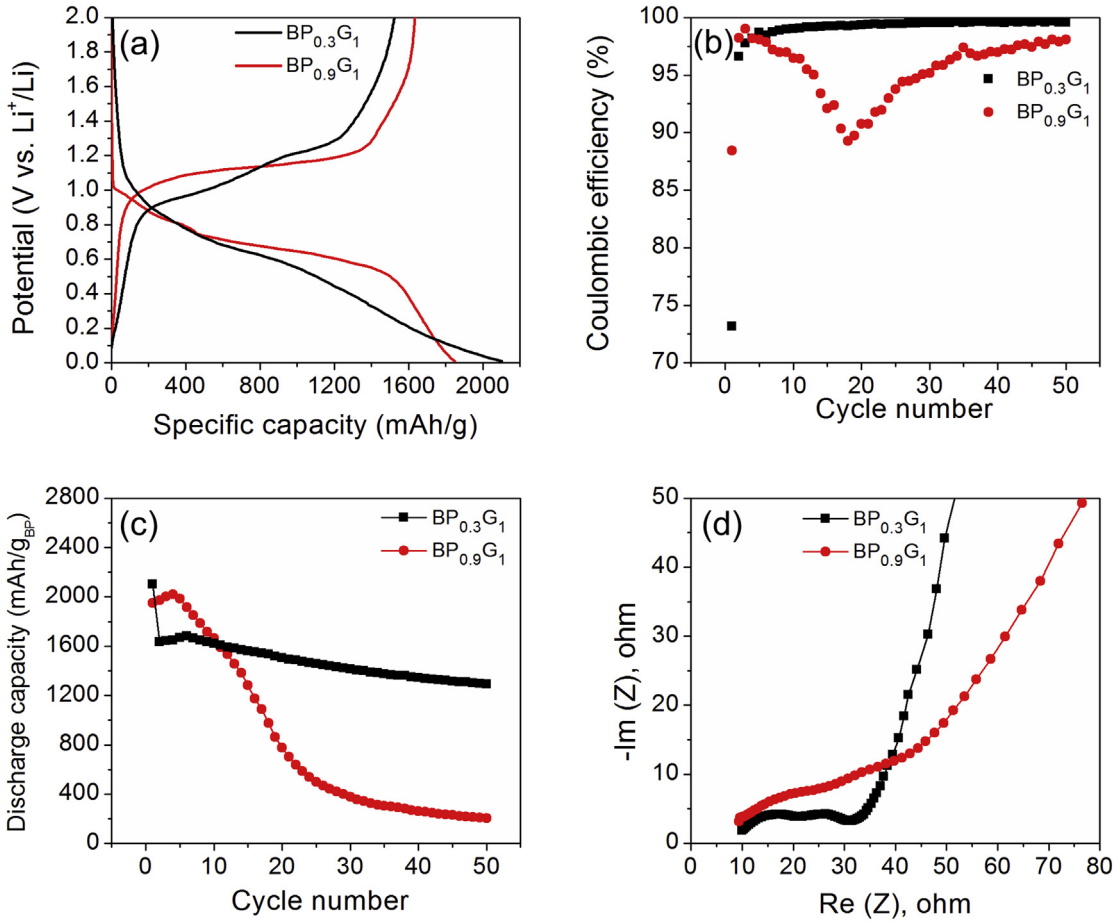

Fig. 6. Comparisons of (a) the 1st cycle discharge-charge profile, (b) coulombic efficiency, (c) cycle performance, and (d) EIS spectra after 50 cycles between $BP_{0.3}G_1$ (black) and $BP_{0.9}G_1$ (red). Half-cells (BP-G vs. Li) were cycled at a current density of 200 mA/g (based on total weight of BP and graphite). (For interpretation of the references to colour in this figure legend, the reader is referred to the Web version of this article.)

cycling. As shown in Fig. 7, the $BP_{0.3}G_1$ electrode maintained its structural integrity after 50 cycles. This means that the $BP_{0.3}G_1$ electrode endured the large volume change while retaining electrical contact between particles. In the cycled $BP_{0.3}G_1$ electrode, cracks in particles or fractured particles were rarely observed (Fig. 7a). The cross-sectional SEM image (Fig. 7c) also revealed that no structural disruption was found in the electrode. In contrast, the $BP_{0.9}G_1$ electrode showed severe mechanical failure at both the particle and electrode level. Cracking of $BP_{0.9}G_1$ particles was considerably found everywhere, and the pulverization of BP-G particles was also observed (Fig. 7b). As a result, the $BP_{0.9}G_1$ electrode was damaged and its structural integrity was not maintained after cycling (Fig. 7d). The mechanical fracture and pulverization led to considerable loss of active materials, followed by loss of electrical contact between active materials. This was confirmed by comparing the EIS spectra of $BP_{0.9}G_1$ and $BP_{0.3}G_1$ after 50 cycles.

As shown in Fig. 6d, while two well-defined and small semicircles in the high and medium frequency ranges were displayed in the case of $BP_{0.3}G_1$, the semicircles were not clearly defined in $BP_{0.9}G_1$ after 50 cycles. Typically, these two suppressed semicircles represent the processes of Li-ion transport through the SEI layer at higher frequencies and the so-called charge-transfer reaction at lower frequencies [25]. The large semicircle at mid-frequency ranges indicates the failure of the interfacial kinetic process in the cell with $BP_{0.9}G_1$, suggesting that the charge transfer reaction barely occurred due to contact loss between $BP_{0.9}G_1$ particles. The large semicircle at high-frequency ranges indicates that $BP_{0.9}G_1$ formed thick SEI layers due to additional SEI formation induced by $BP_{0.9}G_1$ particle crack/fracture/pulverization. This was further confirmed by the change in coulombic efficiency of $BP_{0.9}G_1$ (Fig. 6b). The coulombic efficiency of $BP_{0.9}G_1$ kept decreasing until 20 cycles due to continuous consumption of Li-ions caused by SEI growth, while the coulombic efficiency of $BP_{0.3}G_1$ reached more than 99% within 10 cycles. Note that $BP_{0.3}G_1$ showed a lower first-cycle coulombic efficiency (73.2%) than $BP_{0.9}G_1$ (88.4%). The large 1st-cycle irreversible capacity loss of $BP_{0.3}G_1$ resulted in the reversible capacity of approximately 1600 mAh/g at a current density of 200 mAh/g. The low first-cycle coulombic efficiency of $BP_{0.3}G_1$ might be due to more formation of the SEI layer or side reactions caused by the large surface area of $BP_{0.3}G_1$. In the previous section, XRD demonstrated that $BP_{0.3}G_1$ exhibited an amorphous-like structure, while $BP_{0.9}G_1$ had a medium-range order structure with original BP characteristics. Powders with an amorphous structure are shown to have a larger specific surface area than the corresponding crystalline powder [26].

The absence of fracture and pulverization of particles in the cycled $BP_{0.3}G_1$ electrode could be correlated with the intrinsic material characteristics of $BP_{0.3}G_1$. This might be explained by the difference in the characteristics of discharge-charge profiles of $BP_{0.9}G_1$ and $BP_{0.3}G_1$. As shown in Fig. 6a, $BP_{0.9}G_1$ showed a relatively long discharge and charge voltage plateau at approximately 0.7 and 1.1 V, respectively, where lithiation and delithiation mainly

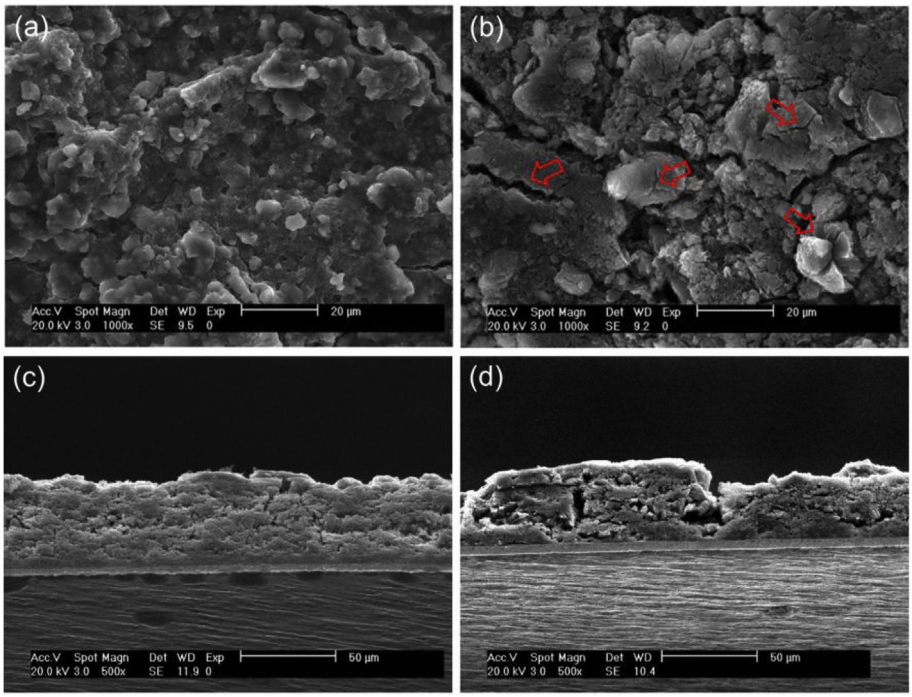

Fig. 7. Top-view and cross-sectional SEM images of (a) (c) $BP_{0.3}G_1$ and (b) (d) $BP_{0.9}G_1$ electrodes after 50 cycles.

occurred. In addition, the discharge curve sharply decreased below the voltage plateau (0.7 V). In contrast, $BP_{0.3}G_1$ exhibited a shorter discharge (lithiation) voltage plateau at approximately 0.7 V and the discharge curve gradually decreased below the voltage plateau. Moreover, $BP_{0.3}G_1$ showed two charge (delithiation) voltage plateaus at approximately 1.0 and 1.2 V. The different characteristics of discharge-charge profiles of $BP_{0.9}G_1$ and $BP_{0.3}G_1$ indicate that the lithiation and delithiation reaction mechanisms could be different.

To further analyze the difference in electrochemical reactions, discharge-charge and the corresponding differential capacity curves of $BP_{0.9}G_1$ were compared with those of $BP_{0.3}G_1$, as shown in Fig. 8. During the first discharge, $BP_{0.9}G_1$ showed several cathodic peaks near 1.0, 0.8, 0.7, and 0.5 V, which correspond to SEI formation (0.8 V) and lithiation-related reactions (0.7 and 0.5 V). The origin of the peak at near 1.0 V was not clear, which was not seen in $BP_{0.3}G_1$, and it disappeared after the first cycle. It could correspond to formation of irreversible Li_xP. Alternatively, several cathodic peaks could be related to lithiation reactions coupled with side reactions induced by particle fracturing and cracking. Note that the peak related to SEI formation (0.8 V, marked with asterisk) was still present during the 3rd cycle, which was different from the case of $BP_{0.3}G_1$. This indicates that additional SEI formation occurred in $BP_{0.9}G_1$ during the 3rd cycle due to newly exposed surface areas of fractured and cracked $BP_{0.9}G_1$ particles. During the 1st and 3rd discharge, $BP_{0.9}G_1$ showed only one anodic peak at 1.1 V, which corresponded to delithiation reaction. During the 25th cycle, the anodic and cathodic peaks were greatly diminished and shifted to the higher and lower voltages, respectively, indicating little lithiation/delithiation and large polarization. In contrast, $BP_{0.3}G_1$ showed only one lithiation-related cathodic peak at near 0.7 V and two delithiation-related anodic peaks at near 1.0 and 1.2 V. The intensity and position of lithiation/delithiation-related peaks remained relatively well during 25 cycles. The SEI formation-related peak at 0.8 V (marked with asterisk) disappeared after the 1st cycle, demonstrating no severe fractures and cracks occurred in $BP_{0.3}G_1$.

The distinct difference in the differential capacity curves suggests that the lithiation/delithiation process of $BP_{0.3}G_1$ is considerably different from $BP_{0.9}G_1$. In particular, it is apparent that the delithiation mechanism of $BP_{0.3}G_1$ (two anodic reactions) is different from $BP_{0.9}G_1$ (one anodic reaction). This could be attributed to the difference in crystal structure of $BP_{0.3}G_1$ and $BP_{0.9}G_1$. $BP_{0.3}G_1$, having an amorphous type of structure with a lot of robust P–C bonds, could cause a unique lithiation/delithiation mechanism that avoids particle fracturing and cracking. Alternatively, it might be a suitable structure form that withstands the large volume change upon cycling. Note that BP suffers from a huge size increase and cracking during delithiation process, not lithiation process [14]. The two-step delithiation process observed in $BP_{0.3}G_1$ may mitigate delithiation-induced stress since the stress is distributed through two electrochemical reaction steps. However, we cannot rule out the possibility that the extra graphite used in $BP_{0.3}G_1$ might act as a flexible buffer matrix during cycling. The extra graphite might allow BP-G microparticles to expand and fractured nanoparticles to anchor while retaining electrical connectivity at both the particle and electrode level [27].

3.4. Other possible failure mechanisms in BP-based anode

As demonstrated, mechanical failure was mainly responsible for the capacity fade observed in BP-based anodes. However, there are still unknown failure/degradation mechanisms that need to be explored. Herein, we briefly discuss two possible mechanisms that might underlie the poor cycle life of BP-based anodes. Although further research will be required to understand how these mechanisms are correlated with the cycle performance of BP-based anodes, it is worthwhile to discuss these issues to have a better understanding of the BP-based anode.

The pristine BP surface is hydrophobic, but it changes to hydrophilic progressively through oxidation [28–30]. It was observed that air moisture can be adsorbed on the surface of BP-based electrodes due to the highly hydrophilic nature of BP. Upon

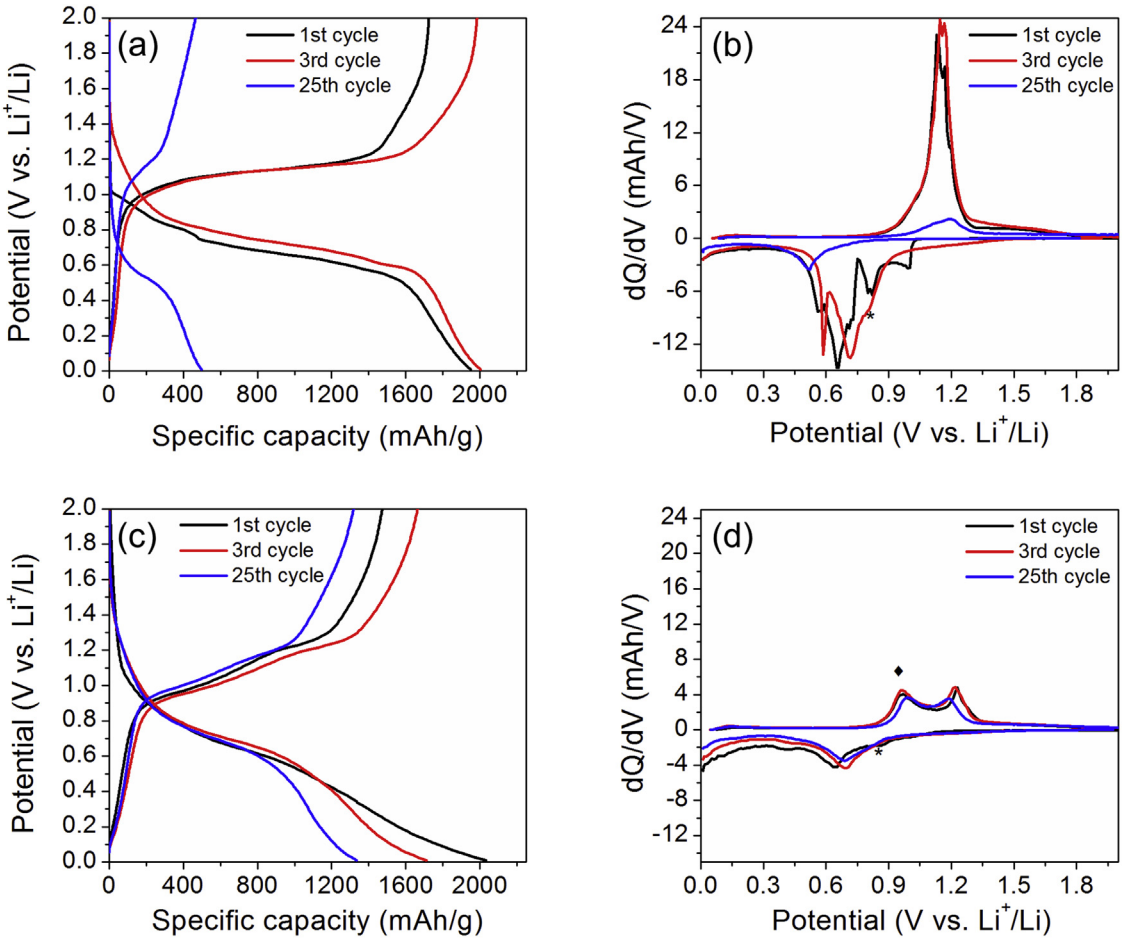

Fig. 8. Galvanostatic discharge-charge profiles and the corresponding differential capacity plots of (a) (b) $BP_{0.9}G_1$ and (c) (d) $BP_{0.3}G_1$ at the 1st, 3rd, and 25th cycle.

exposure to air, the smooth surface of BP electrode changes to an extremely rough surface with many defects. However, the BP electrode stored in an Ar-filled glove box did not show any changes in the surface (Fig. S5). This suggests that the BP-based anode is prone to degrade upon exposure to ambient conditions. It should be mentioned that the adsorption behavior of the BP electrode occurred in a short period of time. As shown in the microscope images (Fig. S6), the surface of BP electrode was blurred quickly because the height of the surface was considerably changed by adsorbing moisture. These results suggest that oxygen and moisture-free synthesis environment is very important to obtain high purity of BP. More importantly, these suggest that the capacity degradation of BP-based anodes might be correlated to the electrode's structural disruption induced by BP's hydrophilic nature upon oxidation. It is generally accepted that a significant amount of oxygen and moisture is generated in a battery cell due to electrolyte decomposition or side reactions. Not only large volume change but also BP's hydrophilic nature by oxidation might affect the mechanical degradation of BP-based anodes. Since $BP_{0.9}G_1$ has a higher amount of BP than $BP_{0.3}G_1$, stronger hydrophilic nature of $BP_{0.9}G_1$ might affect the mechanical degradation. In fact, we observed that the cycled $BP_{0.9}G_1$ electrode was severely wrinkled and bent upon exposure to air.

Formation of Cu_3P might be another reason for the mechanical failure of BP-based electrodes. As discussed in a previous study [12], the electrode preparation procedure should be done carefully to avoid the formation of Cu_3P on the Cu current collector. In our study, we found that electrode drying temperature and time, BP particle size, and the type of binder contribute to the formation of Cu_3P in the BP-based anode (Fig. S7). At the particle level, the formation of Cu_3P might be beneficial in terms of electrochemical performance since Cu_3P is also an electrochemically active material with lithium. At the electrode level, however, the formation of Cu_3P could be detrimental in terms of mechanical stability of the electrode. It was observed that the significant formation of Cu_3P phase wrinkles the BP-based electrode and causes many defects. This might be due to the strong attraction force induced by locally formed Cu_3P in the BP electrode. It is worthwhile to mention that more attention should be paid to P-C composites with a high ratio of P when the electrode is made. Since a P-C composite with a high content of P (like $BP_{0.9}G_1$) contains a considerable amount of P, it is more susceptible to Cu_3P phase formation than a P-C composite with a low ratio of P. Further studies are needed to understand the correlation between Cu_3P formation and the mechanical degradation of BP-based electrodes.

4. Conclusions

We have systematically investigated the difference between BP-G composite with a high ratio of BP ($BP_{0.9}G_1$) and BP-G composite with a low ratio of BP ($BP_{0.3}G_1$) to understand the correlation between material property and electrochemical performance. The results demonstrate the significance of BP-G composition for achieving cycle stability of the BP-G composite. We found that the

crystal structure and P–C bonds of BP-G composites are affected by BP:G molar ratio, which determines the structural integrity of BP-G composites. $BP_{0.3}G_1$ composite has a structurally-stable crystal structure with considerable P–C bonds, which is beneficial for withstanding the large volume change during cycling. Moreover, it results in a different lithiation/delithiation mechanism during cycling. As a result, stable cycle performance can be achieved with the $BP_{0.3}G_1$ composite. In contrast, $BP_{0.9}G_1$ composite cannot avoid fast capacity fade mainly caused by the fracture and pulverization during cycling because it has less structural stability than $BP_{0.3}G_1$. The difference in the structural characteristics of BP-G composites caused by BP-G molar ratio is directly correlated to the differences in their electrochemical performance and lithiation/delithiation mechanism.

We suggest other possible mechanisms underlying capacity degradation of BP-based anode materials. Both highly hydrophilic nature of BP upon oxidation and formation of Cu_3P phase on Cu current collector might contribute to additional structural instability of BP-based electrodes.

This work provides a better understanding of black phosphorus-graphite composite materials and its mechanical degradations, which establish a fundamental framework to develop strategies for synthesizing better materials.

Acknowledgments

This research was supported by SAMSUNG Global Research Outreach (GRO) program. The authors gratefully acknowledge the support.

Appendix A. Supplementary data

Supplementary data to this article can be found online at https://doi.org/10.1016/j.electacta.2019.03.149.

References

[1] L. Sun, M. Li, K. Sun, S. Yu, R. Wang, H. Xie, J. Phys. Chem. C 116 (2012) 14772.
[2] J. Sun, G. Zheng, H. Lee, N. Liu, H. Wang, H. Yao, W. Yang, Y. Cui, Nano Lett. 14 (2014) 4573.
[3] Y. Kim, Y. Park, A. Choi, N. Choi, J. Kim, J. Lee, J. Ryu, S. Oh, K. Lee, Adv. Mater. 25 (2013) 3045.
[4] Q. Jiang, L. Xu, N. Chen, H. Zhang, L. Dai, S. Wang, Angew. Chem. Int. Ed. 55 (2016) 13849–13853.
[5] X. Ren, Z. Li, Z. Huang, D. Sang, H. Qiao, X. Qi, J. Li, J. Zhong, H. Zhang, Adv. Funct. Mater. 27 (2017), 1606834.
[6] X. Ren, J. Zhou, X. Qi, Y. Liu, Z. Huang, Z. Li, Y. Ge, S. Dhanabalan, J. Ponraj, S. Wang, J. Zhong, H. Zhang, Adv. Energy Mater. 7 (2017) 1700396.
[7] C. Marino, L. Boulet, P. Gaveau, B. Fraisse, L. Monconduit, J. Mater. Chem. 22 (2012) 22713.
[8] J. Qian, D. Qiao, X. Ai, Y. Cao, H. Yang, Chem. Commun. 48 (2012) 8931.
[9] L. Wang, X. He, J. Li, W. Sun, J. Gao, J. Guo, C. Jiang, Angew. Chem. Int. Ed. 51 (2012) 9034.
[10] J. Song, Z. Yu, M.L. Gordin, S. Hu, R. Yi, D. Tang, T. Walter, M. Regula, D. Choi, X. Li, A. Manivannan, D. Wang, Nano Lett. 14 (2014) 6329.
[11] C. Park, H. Sohn, Adv. Mater. 19 (2007) 2465.
[12] M. Stan, J. Zamory, S. Passerini, T. Nilges, M. Winter, J. Mater. Chem. A 1 (2013) 5293.
[13] J. Sun, H. Lee, M. Pasta, H. Yuan, G. Zheng, Y. Sun, Y. Li, Y. Cui, Nat. Nanotechnol. 10 (2015) 980.
[14] W. Xia, Q. Zhang, F. Xu, H. Ma, J. Chen, K. Qasim, B. Ge, C. Zhu, L. Sun, J. Phys. Chem. C 120 (2016) 5861.
[15] Y. Wang, L. Tian, Z. Yao, F. Li, S. Li, S. Ye, Electrochem. Acta 163 (2015) 71.
[16] J. Li, L. Wang, X. He, J. Wang, ACS Sustain. Chem. Eng. 4 (2016) 4217.
[17] T. Ramireddy, T. Xing, M. Rahman, Y. Chen, Q. Dutercq, D. Gunzelmann, A. Glushenkov, J. Mater. Chem. A 3 (2015) 5572.
[18] M. Nagao, A. Hayashi, M. Tatsumisago, J. Power Sources 196 (2011) 6902.
[19] H. Liu, Y. Du, Y. Deng, P. Ye, Chem. Soc. Rev. 44 (2015) 2732.
[20] L. Hardwick, M. Marcinek, L. Beer, J.B. Kerr, R. Kostecki, J. Electrochem. Soc. 155 (2008) A442.
[21] F. Claeyssens, G. Fuge, N. Allan, P. May, M. Ashfold, Dalton Trans. 0 (2004) 3085.
[22] F. Claeyssens, Phys. Rev. B 79 (2009), 134115.
[23] J. Hart, N. Allan, F. Claeyssens, Phys. Chem. Chem. Phys. 12 (2010) 8620.
[24] A. Mauger, C. Julien, Nanomaterials 5 (2015) 2279.
[25] H. Shin, J. Park, A. Sastry, W. Lu, J. Electrochem. Soc. 162 (2015) A1683.
[26] H. Jia, J. Stark, L. Zhou, C. Ling, T. Sekito, Z. Markin, RSC Adv. 2 (2012) 10874.
[27] X. Han, H. Chen, Z. Zhang, D. Huang, J. Xu, C. Li, S. Chen, Y. Yang, J. Mater. Chem. A 4 (2016) 17757.
[28] Y. Huang, J. Qiao, K. He, S. Bliznakov, E. Sutter, X. Chen, D. Luo, F. Meng, D. Su, J. Decker, W. Ji, R. Ruoff, P. Sutter, Chem. Mater. 28 (2016) 8330.
[29] P. Yasaei, A. Behranginia, T. Foroozan, M. Asadi, K. Kim, F.K. Araghi, A.S. Khojin, ACS Nano 9 (2015) 9898.
[30] A. Gomez, L. Vicarelli, E. Prada, J. Island, K.L. Narasimha-Acharya, S.I. Blanter, D.J. Groenendijk, M. Buscema, G.A. Steele, J.V. Alvarez, H.W. Zandbergen, J.J. Palacios, H.S.J. van der Zant, 2D Mater. 1 (2014), 025001.